Anisotropic non-equilibrium lattice dynamics of black phosphorus

Daniela Zahn, Patrick-Nigel Hildebrandt, Thomas Vasileiadis,
Yoav William Windsor, Yingpeng Qi, Hélène Seiler, and Ralph Ernstorfer
Fritz Haber Institute of the Max Planck Society, Faradayweg 4-6, 14195 Berlin, Germany

Black phosphorus has recently attracted significant attention for its highly anisotropic properties. A variety of ultrafast optical spectroscopies has been applied to probe the carrier response to photoexcitation, but the complementary lattice response has remained unaddressed. Here we employ femtosecond electron diffraction to explore how the structural anisotropy impacts the lattice dynamics after photoexcitation. We observe two timescales in the lattice response, which we attribute to electron-phonon and phonon-phonon thermalization. Pronounced differences between armchair and zigzag directions are observed, indicating a non-thermal state of the lattice lasting up to ~ 60 picoseconds. This non-thermal state is characterized by a modified anisotropy of the atomic vibrations compared to equilibrium. Our findings provide insights in both electron-phonon as well as phonon-phonon coupling and bear direct relevance for any application of black phosphorus in non-equilibrium conditions.

Layered van der Waals (vdW) materials have attracted significant research interest in recent years due to their potential device applications [1–4]. The most prominent 2D material, graphene, exhibits high carrier mobility, but lacks a band gap, which is required in many applications. In contrast, transition metal dichalcogenides possess a band gap in the visible range, but a lower carrier mobility. With a thickness-dependent band gap extending from the infrared to the visible [5–7] and a high carrier mobility [8–10], black phosphorus provides an important complementary building block for vdW heterostructure devices. A central aspect of black phosphorus is its in-plane anisotropic structure, shown in Figure 1a. The layers have two inequivalent high-symmetry directions, the so-called zigzag and armchair directions. This structural anisotropy is also reflected in many macroscopic material properties, such as optical absorption [9, 11–14] and in-plane anisotropic thermal [15–18] and electrical [5, 9, 19, 20] conductivities. These anisotropic properties offer additional tunability in device design.

Since any device operates in non-equilibrium conditions, a microscopic understanding of non-equilibrium states in vdW materials is of particular interest. For optoelectronic devices, knowledge of the evolution of the system after optical excitation is desired. Carrier dynamics in black phosphorus have been studied using a variety of time-resolved optical spectroscopies [20–26] as well as time- and angle-resolved photoemission [27, 28]. An important relaxation pathway for excited carriers is via coupling to the lattice. However, to date, no study has directly reported on the ultrafast lattice response of black phosphorus upon photoexcitation, which reflects the strength of electron-phonon as well as phonon-phonon interaction. In this work, we employ femtosecond electron diffraction [29] (FED) to directly probe the structural dynamics of photoexcited black phosphorus.

The measurement principle is sketched in Figure 1b. The sample is excited with an ultrashort laser pulse (pump) and the lattice response is probed using an ultrashort electron pulse (probe) with a kinetic energy of 70 keV. The electrons are diffracted by the sample and

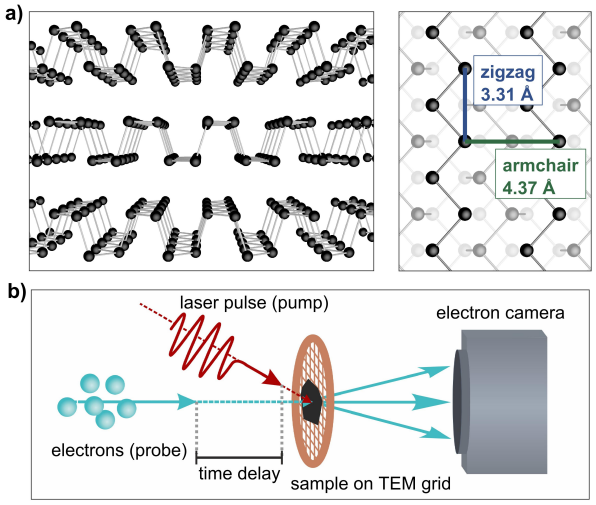

Figure 1. Anisotropic structure of black phosphorus and schematic illustration of the experiment. (a) Side and top view of the crystal structure of black phosphorus, showing anisotropy not only between the in-plane and out-of-plane directions, but also between the in-plane directions (armchair and zigzag). (b) Schematic representation of a time-resolved electron diffraction setup (see text for details).

diffraction patterns are recorded in transmission for different time delays between pump and probe pulse. To excite the sample, we use optical pulses with a wavelength of 770 nm (1.61 eV). The polarization of the pump pulse is set to the armchair direction of the crystal. All measurements are performed at a base temperature of 100 K.

Since diffraction patterns are measured in transmission, the samples need to be thin films. We prepared a thin film of black phosphorus by mechanical exfoliation from a bulk crystal (*HQ Graphene*) using water-soluble glue and transferred it on a standard copper TEM grid using the floating technique [30]. Based on the transmission of the film and previously reported optical constants of black phosphorus [14], we estimate the film thickness

to be 39 ± 5 nm. The sample was transferred to vacuum directly after preparation to minimize degradation.

Figure 2a shows a typical transmission diffraction pattern of black phosphorus. The orthorhombic crystal structure of black phosphorus (see Figure 1a) results in an anisotropic diffraction pattern. Bragg reflections along the zigzag and armchair directions, (h00) and (00l), are marked with blue and green boxes, respectively. Only reflections with even h and l are allowed due to the crystal symmetry (space group Cmce with phosphorus atoms at Wyckoff positions 8f). We observe additional forbidden reflections caused by stacking faults, multiple scattering, or structural deviations at the surfaces, which are not taken into account in the following analysis.

In this work, we focus on the Bragg reflections along the armchair and zigzag directions. Our primary observables are the intensities of the Bragg reflections, which decrease with increasing displacement of the atoms due to lattice vibrations (Debye-Waller effect). Since the probe electrons propagate in parallel to the van der Waals stacking direction through the crystal, our measurement is sensitive to the in-plane atomic vibrations.

To extract intensities from the diffraction patterns, we fit the observed peaks to the sum of a 2D pseudo-Voigt profile and a tilted background. The same Gaussian-Lorenzian mixing is assumed in all directions. The integrated intensity of the peak is then used to obtain the intensity change as function of pump-probe delay. Figure 2b displays the resulting evolution of the Bragg reflection intensities after photoexcitation. We observe two timescales in the intensity decrease and pronounced differences between reflections along the armchair and zigzag directions. The amplitudes of the intensity decrease are larger for reflections with higher scattering vectors, as expected by Debye-Waller theory.

To analyze the structural dynamics, we convert the Bragg reflection intensities into change in atomic mean squared displacement (MSD). For anisotropic crystals, the temperature factor is: [31–33]

$$\tau = \exp\{-\frac{1}{2}[U_{11}(ha^*)^2 + U_{22}(kb^*)^2 + U_{33}(lc^*)^2 + \\ +2U_{12}ha^*kb^* + 2U_{23}kb^*lc^* + 2U_{13}ha^*lc^*]\} \quad (1)$$

Here, h,k and l are the Miller indices and a^*,b^* and c^* are the magnitudes of the reciprocal space lattice vectors, defined such that $\mathbf{a} \cdot \mathbf{a}^* = 2\pi$. For black phosphorus in the standard setting of Cmce, $\mathbf{a}, \mathbf{b}, \mathbf{c}$ are the (real space) lattice vectors in zigzag (a=3.31 Å), out-of-plane (b=10.46 Å) and armchair (c=4.37 Å) directions [34]. U_{11},U_{22} and U_{33} correspond to the MSDs in zigzag, out-of-plane, and armchair direction, respectively (see references [31, 32] for more details about the U-matrix). Note that in black phosphorus, U_{12} and U_{13} are zero due to symmetry [34, 35]. For Bragg reflections purely along the zigzag direction, that is (h00), the relative intensity change after laser excitation is given by:

$$\frac{I(t)}{I_0} = \exp\{-[U_{11}(t) - U_{11}^0]\frac{4\pi^2}{a^2}h^2)\} \quad (2)$$

Similarly, for reflections purely along the armchair direction, (00l), the relative intensity change after laser excitation reads:

$$\frac{I(t)}{I_0} = \exp\{-[U_{33}(t) - U_{33}^0]\frac{4\pi^2}{c^2}l^2)\} \quad (3)$$

Here, U_{ii}^0 denotes the MSD before laser excitation and $U_{ii}(t)$ denotes the MSD as function of pump-probe delay. $I(t)$ denotes the intensity as function of pump-probe delay and I_0 is the intensity before laser excitation.

The changes in MSD, shown in Figure 2c, are markedly different for the armchair and zigzag directions. From the different amplitudes we conclude that the interatomic potential is anisotropic. It is energetically less costly to displace atoms along the armchair direction compared to the zigzag direction. Hence, as the lattice temperature rises, the additional energy leads to a larger increase of the MSD in the armchair direction. These findings are in qualitative agreement with lattice dynamical calculations [36] and static X-ray diffraction measurements [34].

To compare the timescales of the lattice dynamics in armchair and zigzag direction qualitatively, we normalize the MSD change to its mean value at 80-100 ps. The result is shown in Figure 2d. For both directions, two timescales are observed in the lattice response, with pronounced differences between armchair and zigzag directions. To analyze these quantitatively, we fit the MSD change (Figure 2c) to a bi-exponential function. The finite time resolution is taken into account by convolving the fit function with a Gaussian kernel with a FWHM of 150 fs. The fit results for the amplitudes A_i and time constants τ_i are summarized in Table I.

	armchair	zigzag
A_1 [10^{-3}Å^2]	0.74 ± 0.03	0.70 ± 0.02
τ_1 [ps]	0.66 ± 0.06	0.53 ± 0.03
A_2 [10^{-3}Å^2]	2.12 ± 0.03	0.89 ± 0.02
τ_2 [ps]	22 ± 1	20 ± 1

Table I. Fit results of the MSD in armchair und zigzag directions with a bi-exponential function convolved with a Gaussian kernel. The errors correspond to 68.3 % confidence intervals of the fit.

The fast time constants τ_1 are very similar for armchair and zigzag directions. We attribute this initial rise of the MSD to energy transfer from the photo-excited electrons to the lattice. The timescales are consistent with time-resolved optical spectroscopy results [23, 24, 26]. The relative amplitude of the fast rise in MSD is higher in the zigzag direction, see Figure 2d. This indicates that electron-phonon equilibration leads to a non-thermal phonon distribution. Compared to the thermal case, this non-thermal phonon distribution is characterized by a higher ratio of the zigzag to armchair MSD. Hence, on average, phonons with a high displacement in zigzag direction couple more strongly to the electrons. On longer timescales, the non-thermal phonon distribution relaxes

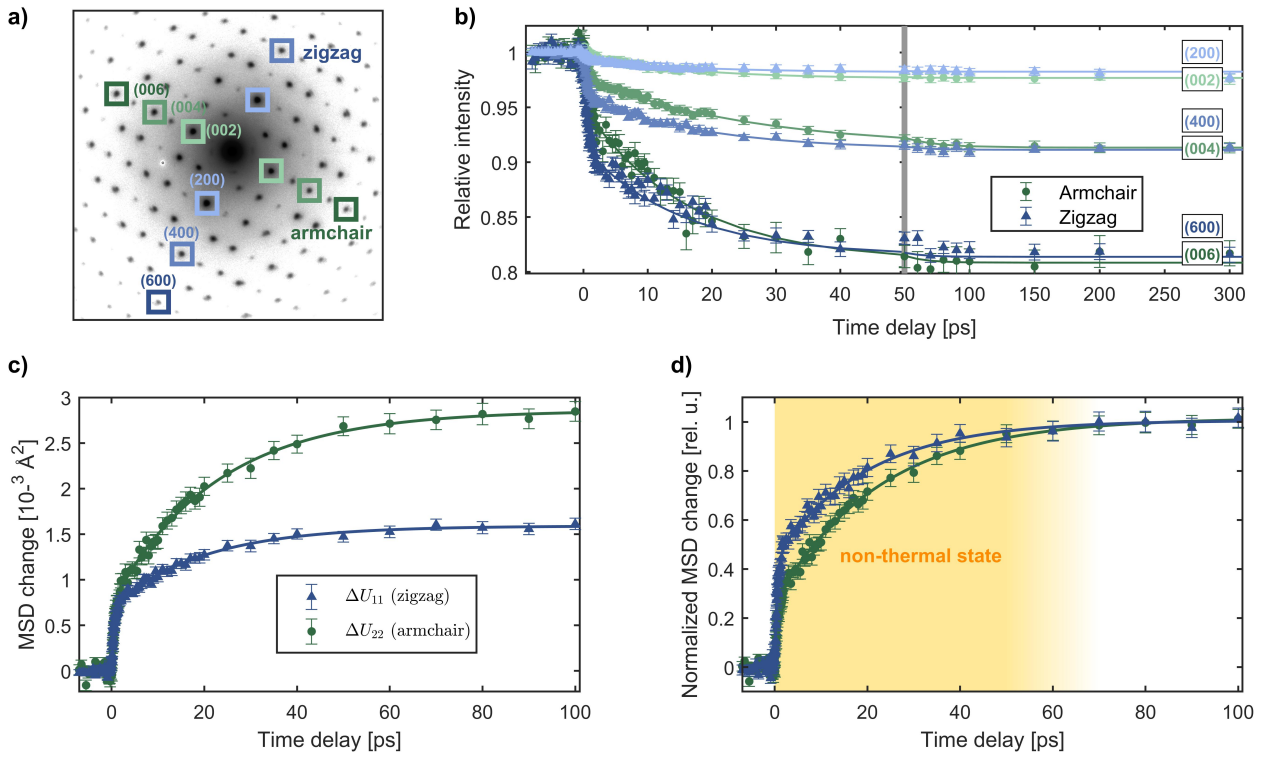

Figure 2. Overview of anisotropic lattice dynamics in photoexcited black phosphorus. (a) Transmission diffraction pattern of thin-film black phosphorus. We focus on the high-symmetry Bragg reflections along the armchair and zigzag directions, indicated by colored boxes. (b) Relative changes in Bragg reflection intensities as function of pump-probe delay. Here, we average over the Friedel pairs, e.g. (002) and $(00\bar{2})$, since they show the same dynamics. The measurement was conducted with an incident fluence of $(9.8 \pm 1.4)\,\mathrm{mJ/cm^2}$. Based on the optical constants of black phosphorus [14] and the film thickness, we estimate the absorbed energy density to be $(380 \pm 70)\,\mathrm{J/cm^3}$. The data presented are the average of several delay scans, and the error estimates represent the standard error of the mean. (c) Change of atomic mean squared displacement (MSD) in the armchair (green circles) and zigzag (blue triangles) directions as function of pump-probe delay. The anisotropy of the lattice is reflected in an anisotropic MSD change in the two directions. The higher MSD change in the armchair direction indicates that bonds are softer in this direction. The MSD values presented are the weighted average of MSDs calculated from each Friedel pair and the error bars are calculated using error propagation. (d) MSD change normalized its mean value at 80-100 ps. A two-step timescale as well as a transient non-equilibrium between the zigzag and armchair directions is observed.

into a thermal phonon distribution. We attribute the second rise of the MSD to these redistribution processes. The fact that the MSD rises further during phonon thermalization indicates that high-energy phonons decay into lower-energy phonons, because one high-energy phonon decays into multiple low-energy phonons and in addition, low-energy phonons produce a higher atomic displacement per phonon [33].

Since the conduction band minimum and the valence band maximum are located at the Z-point of the Brillouin zone [5], thermalized carriers can absorb and emit mostly phonons with small momenta. Hence, we can conclude that lattice thermalization is achieved mostly by direct phonon-phonon coupling via anharmonicities. Finally, a thermal state is reached after ~ 60 ps. This timescale of phonon-thermalization is similar to timescales reported for the vdW materials WSe_2 [37] and graphite [38]. In contrast to these materials, however, the non-thermal phonon population in black phosphorous manifests itself in an anisotropic evolution of the MSD due to the in-plane anisotropy. We performed similar experiments with the pump pulses polarized along the zigzag direction of the samples (not shown in this letter). Within the experimental uncertainty, we observe the same biexponential dynamics of the Bragg reflections, while the amplitude of the photo-induced signal is reduced by $\sim 75\%$ due to the anisotropic optical absorption.

So far, we have only considered the MSD along armchair and zigzag directions. However, we can calculate the MSD along all in-plane directions based on the MSD along these two directions [31, 35]. Figure 3 visualizes the evolution of the in-plane MSD, using the bi-exponential fit of the data shown in Figure 2c and the estimated temperature rise of (270 ± 50) K [39].

In equilibrium, the shape of the in-plane MSD is already anisotropic (blue curves of Figure 3) due to the anisotropic bond stiffness. After laser-excitation, the MSD increases as shown in Figure 2c. The evolution

of the MSD is displayed in Figure 3a. Note that not only the size, but also the shape of the MSD evolves with time. This is visualized in Figure 3b by showing the MSD curves normalized to their area. The non-thermal phonon distribution leads to a transient reduction of the MSD anisotropy, with a larger MSD in zigzag direction compared to equilibrium. On longer timescales, as the phonons thermalize, the MSD relaxes back to its equilibrium shape (dashed red curve).

In summary, our measurements have explored how structural anisotropy impacts lattice thermalization in photoexcited black phosphorus. We have shown that the lattice response is well captured by a bi-exponential decay: a sub-ps component, common to both zigzag and armchair Bragg reflections, is assigned to electron-phonon equilibration, while a ~ 20 ps component is found to be highly anisotropic and indicative of a non-thermal phonon population persisting for ~ 60 ps. Our analysis reveals that the non-thermal phonon population results in a transient shape change of the MSD, with a higher displacement in zigzag direction compared to equilibrium.

We expect this non-thermal state of the lattice to have effects on the macroscopic properties of black phosphorus, such as thermal and electrical conductivities. In particular, for any application in which hot carriers are excited or injected in black phosphorus, transient changes of material properties will influence device performance. Beyond black phosphorus, we expect these results to be relevant to other vdW materials as well. For example, in any layered material, the evolution of in-plane and out-of-plane MSD could be different, with implications for energy flow across heterostructure interfaces.

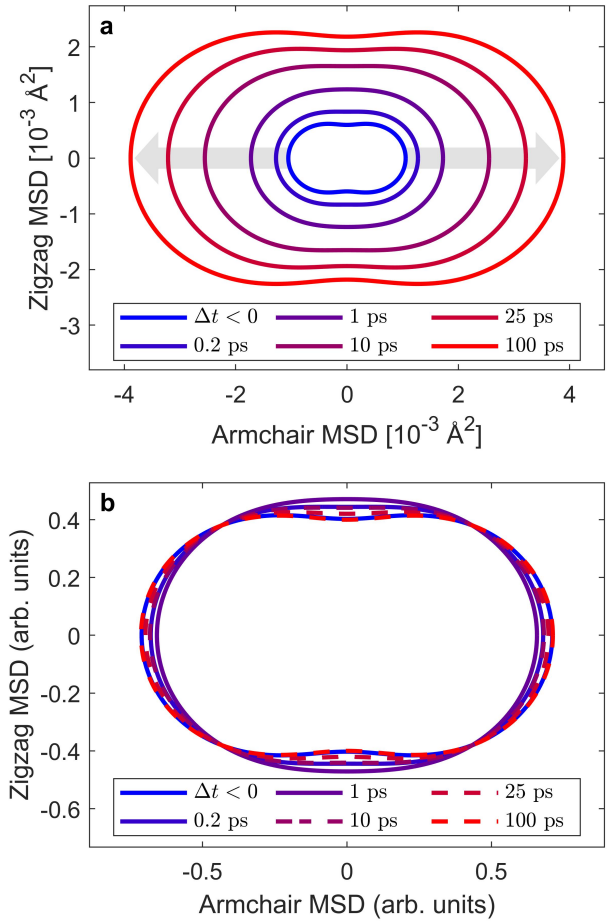

Figure 3. Photoexcitation transiently modifies the anisotropy of the atomic mean square displacement (MSD). (a) Evolution of the MSD from before excitation (blue) to the thermalized state at 100 ps (red). The shape of the in-plane MSD before laser-excitation is already anisotropic due to the in-plane structural anisotropy. Note that the MSD increases due to lattice heating, but also the shape of the MSD changes transiently. (b) MSD curves from Panel (a), normalized to their area. This highlights the transient shape change of the MSD due to a non-thermal phonon distribution.

I. ACKNOWLEDGEMENT

This work was funded by the Max Planck Society and the European Research Council (ERC) under the European Unions Horizon 2020 research and innovation program (Grant Agreement Number ERC-2015-CoG-682843). H.S. acknowledges support by the Swiss National Science Foundation under Grant No. P2SKP2_184100. Y.Q. acknowledges support by the Sino-German (CSC-DAAD) Postdoc Scholarship Program (Grant No. 57343410).

[1] Lotsch, B. V. *Annu. Rev. Mater. Res.* **2015**, *45*, 85–109.
[2] Novoselov, K. S.; Mishchenko, A.; Carvalho, A.; Castro Neto, A. H. *Science* **2016**, *353*, aac9439.
[3] Schulman, D. S.; Arnold, A. J.; Razavieh, A.; Nasr, J.; Das, S. *IEEE Nanotechnol. Mag.* **2017**, *11*, 6–17.
[4] Cheng, J.; Wang, C.; Zou, X.; Liao, L. *Adv. Opt. Mater.* **2019**, *7*, 1800441.
[5] Qiao, J.; Kong, X.; Hu, Z.-X.; Yang, F.; Ji, W. *Nat. Commun.* **2014**, *5*, 4475.
[6] Castellanos-Gomez, A. *J. Phys. Chem. Lett.* **2015**, *6*, 4280–4291.
[7] Li, L. et al. *Nat. Nanotechnol.* **2017**, *12*, 21–25.
[8] Li, L.; Yu, Y.; Ye, G. J.; Ge, Q.; Ou, X.; Wu, H.; Feng, D.; Chen, X. H.; Zhang, Y. *Nat. Nanotechnol.* **2014**, *9*, 372–377.
[9] Xia, F.; Wang, H.; Jia, Y. *Nat. Commun.* **2014**, *5*, 4458.
[10] Long, G.; Maryenko, D.; Shen, J.; Xu, S.; Hou, J.; Wu, Z.; Wong, W. K.; Han, T.; Lin, J.; Cai, Y.; Lortz, R.; Wang, N. *Nano Lett.* **2016**, *16*, 7768–7773.
[11] Tran, V.; Soklaski, R.; Liang, Y.; Yang, L. *Phys. Rev. B* **2014**, *89*, 235319.
[12] Low, T.; Rodin, A. S.; Carvalho, A.; Jiang, Y.; Wang, H.; Xia, F.; Castro Neto, A. H. *Phys. Rev. B* **2014**, *90*, 075434.
[13] Lan, S.; Rodrigues, S.; Kang, L.; Cai, W. *ACS Photonics* **2016**, *3*, 1176–1181.
[14] Jiang, H.; Shi, H.; Sun, X.; Gao, B. *ACS Photonics* **2018**, *5*, 2509–2515.
[15] Lee, S. et al. *Nat. Commun.* **2015**, *6*, 8573.
[16] Luo, Z.; Maassen, J.; Deng, Y.; Du, Y.; Garrelts, R. P.; Lundstrom, M. S.; Ye, P. D.; Xu, X. *Nat. Commun.* **2015**, *6*, 8572.
[17] Jang, H.; Wood, J. D.; Ryder, C. R.; Hersam, M. C.; Cahill, D. G. *Adv. Mater.* **2015**, *27*, 8017–8022.
[18] Sun, B.; Gu, X.; Zeng, Q.; Huang, X.; Yan, Y.; Liu, Z.; Yang, R.; Koh, Y. K. *Adv. Mater.* **2017**, *29*, 1603297.
[19] Liu, H.; Neal, A. T.; Zhu, Z.; Luo, Z.; Xu, X.; Tomnek, D.; Ye, P. D. *ACS Nano* **2014**, *8*, 4033–4041.
[20] He, J.; He, D.; Wang, Y.; Cui, Q.; Bellus, M. Z.; Chiu, H.-Y.; Zhao, H. *ACS Nano* **2015**, *9*, 6436–6442.
[21] Ge, S.; Li, C.; Zhang, Z.; Zhang, C.; Zhang, Y.; Qiu, J.; Wang, Q.; Liu, J.; Jia, S.; Feng, J.; Sun, D. *Nano Lett.* **2015**, *15*, 4650–4656.
[22] Suess, R. J.; Jadidi, M. M.; Murphy, T. E.; Mittendorff, M. *Appl. Phys. Lett.* **2015**, *107*, 081103.
[23] Wang, K.; Szydowska, B. M.; Wang, G.; Zhang, X.; Wang, J. J.; Magan, J. J.; Zhang, L.; Coleman, J. N.; Wang, J.; Blau, W. J. *ACS Nano* **2016**, *10*, 6923–6932.
[24] Iyer, V.; Ye, P.; Xu, X. *2D Mater.* **2017**, *4*, 021032.
[25] Liao, B.; Zhao, H.; Najafi, E.; Yan, X.; Tian, H.; Tice, J.; Minnich, A. J.; Wang, H.; Zewail, A. H. *Nano Lett.* **2017**, *17*, 3675–3680.
[26] Meng, S.; Shi, H.; Jiang, H.; Sun, X.; Gao, B. *J. Phys. Chem. C* **2019**, *123*, 20051–20058.
[27] Roth, S.; Crepaldi, A.; Puppin, M.; Gatti, G.; Bugini, D.; Grimaldi, I.; Barrilot, T. R.; Arrell, C. A.; Frassetto, F.; Poletto, L.; Chergui, M.; Marini, A.; Grioni, M. *2D Mater.* **2019**, *6*, 031001.
[28] Chen, Z.; Dong, J.; Papalazarou, E.; Marsi, M.; Giorgetti, C.; Zhang, Z.; Tian, B.; Rueff, J.-P.; Taleb-Ibrahimi, A.; Perfetti, L. *Nano Lett.* **2019**, *19*, 488–493.
[29] Waldecker, L.; Bertoni, R.; Ernstorfer, R. *J. Appl. Phys.* **2015**, *117*, 044903.
[30] Dwyer, J. R.; Jordan, R. E.; Hebeisen, C. T.; Harb, M.; ernstorfer, R.; Dartigalongue, T.; Miller, R. J. D. *J. Mod. Opt.* **2007**, *54*, 923–942.
[31] Trueblood, K. N.; Brgi, H.-B.; Burzlaff, H.; Dunitz, J. D.; Gramaccioli, C. M.; Schulz, H. H.; Shmueli, U.; Abrahams, S. C. *Act. Cryst. A* **1996**, *52*, 770–781.
[32] Giacovazzo, C.; Monaco, H. L.; Artioli, G.; Viterbo, D.; Ferraris, G.; Gilli, G.; Zanotti, G.; Catti, M. *Fundamentals of Crystallography*; Oxford University Press, 2002.
[33] Peng, L.; Dudarev, S.; Whelan, M. *High-Energy Electron Diffraction and Microscopy*; Oxford Science Publications, 2011.
[34] Akai, T.; Endo, S.; Akahama, Y.; Koto, K.; Marljyama, Y. *High Press. Res.* **1989**, *1*, 115–130.
[35] Willis, B.; Pryor, A. *Thermal Vibrations in Crystallography*; Cambridge University Press, 1975.
[36] Kaneta, C.; Katayama-Yoshida, H.; Morita, A. *J. Phys. Soc. Japan* **1986**, *55*, 1213–1223.
[37] Waldecker, L.; Bertoni, R.; Huebener, H.; Brumme, T.; Vasileiadis, T.; Zahn, D.; Rubio, A.; Ernstorfer, R. *Phys. Rev. Lett.* **2017**, *119*, 036803.
[38] Stern, M. J.; René de Cotret, L. P.; Otto, M. R.; Chatelain, R. P.; Boisvert, J.-P.; Sutton, M.; Siwick, B. J. *Phys. Rev. B* **2018**, *97*, 165416.
[39] Here we make the assumption that both before and after laser excitation, the MSD is proportional to the temperature (high-temperature limit). To estimate the temperature of the system after electron-lattice equilibration, we use the calculated absorbed energy density and the heat capacity of black phosphorus. The total heat capacity is approximated by its main contribution, the lattice heat capacity, calculated from the vibrational DOS [40].
[40] Machida, Y.; Subedi, A.; Akiba, K.; Miyake, A.; Tokunaga, M.; Akahama, Y.; Izawa, K.; Behnia, K. *Sci. Adv.* **2018**, *4*, eaat3374.